Title: KHS101 disrupts energy metabolism in human glioblastoma cells and reduces tumor growth in mice

Authors: Euan S. Polson[1,†], Verena B. Kuchler[1,†], Christopher Abbosh[1,9], Edith M. Ross[2], Ryan K. Mathew[1,3], Hester A. Beard[4], Bárbara da Silva[1], Andrew N. Holding[2], Stephane Ballereau[2], Eulashini Chuntharpursat-Bon[1], Jennifer Williams[1], Hollie B.S. Griffiths[6], Hao Shao[5], Anjana Patel[1], Adam J. Davies[1], Alastair Droop[1], Paul Chumas[3], Susan C. Short[1], Mihaela Lorger[1], Jason E. Gestwicki[5], Lee D. Roberts[1], Robin S. Bon[1,4], Simon J. Allison[6], Shoutian Zhu[7, 8], Florian Markowetz[2], and Heiko Wurdak[1,*]

Affiliations:

[1] School of Medicine, University of Leeds, Leeds, LS2 9JT, UK.

[2] Cancer Research UK Cambridge Institute, University of Cambridge, Cambridge, CB2 0RE, UK.

[3] Department of Neurosurgery, Leeds General Infirmary, Leeds, LS1 3EX, UK

[4] School of Chemistry, University of Leeds, Leeds, LS2 9JT, UK.

[5] Department of Pharmaceutical Chemistry and the Institute for Neurodegenerative Disease, University of California at San Francisco, 675 Nelson Rising Ln., San Francisco, California 94158, USA.

[6] School of Applied Sciences, University of Huddersfield, Huddersfield, HD1 3DH, UK.

[7] California Institute for Biomedical Research, 11119 North Torrey Pines Road, Suite 100, La Jolla, CA 92037, USA

[8] Current address: Regulus Therapeutics Inc, 10614 Science Center Drive, San Diego, CA 92121, USA

[9] Current address: Cancer Research UK Lung Cancer Centre of Excellence London and Manchester, University College London Cancer Institute, 72 Huntley Street, London WC1E 6DD, UK

* To whom correspondence should be addressed: Heiko Wurdak, Leeds Institute of Cancer and Pathology, School of Medicine, University of Leeds, Leeds LS9 7TF, UK. Phone: 113-343-8636; E-mail: h.wurdak@leeds.ac.uk

† Euan S. Polson and Verena B. Kuchler contributed equally to this work.

Related Resources:

http://stm.sciencemag.org/content/10/448/eaar2238

http://stm.sciencemag.org/content/10/443/eaah6816

http://stm.sciencemag.org/content/10/430/eaao2731

http://stm.sciencemag.org/content/10/422/eaam7577

Overline: Brain tumors

One Sentence Summary

Modulation of energy metabolism with the small molecule KHS101 promoted tumor-selective death of human glioblastoma cells and reduced tumor growth in mice.

Abstract

Pharmacological inhibition of uncontrolled cell growth with small molecule inhibitors is a potential strategy for treating glioblastoma multiforme (GBM), the most malignant primary brain cancer. Here, we showed that the synthetic small molecule KHS101 promoted tumor cell death in diverse GBM cell models, independent of their tumor subtype, and without affecting the viability of non-cancerous brain cell lines. KHS101 exerted cytotoxic effects by disrupting the mitochondrial chaperone heat shock protein family D member 1 (HSPD1). In GBM cells, KHS101 promoted aggregation of proteins regulating mitochondrial integrity and energy metabolism. Mitochondrial bioenergetic capacity and glycolytic activity were selectively impaired in KHS101-treated GBM cells. In two intracranial patient-derived xenograft tumor

models in mice, systemic administration of KHS101 reduced tumor growth and increased survival without discernible side effects. These findings suggest that targeting of HSPD1-dependent metabolic pathways might be an effective strategy for treating GBM.

Introduction

Glioblastoma (GBM) is the most common malignant primary brain tumor in adults and among the most devastating cancers (1). Its overall median time to recurrence after surgery and standard chemoradiotherapy is ~7 months and the 5-year survival rate remains low (<5%) (2). Pre-clinical data have shown that small molecules hold therapeutic promises for treating GBM through perturbation of cell death programs (3), epigenetic and transcriptional pathways (4, 5), lethal autophagy (6), and GBM stem cell self-renewal (7). However, GBM biology remains poorly understood and there is an unmet need for the identification of new targets and the development of alternative therapeutic strategies (2). Although presenting several challenges, phenotypic drug discovery and profiling using small molecules have the advantage of addressing the complexity of diseases, in particular, when the molecular target(s) and the underlying mechanisms of action of a small molecule are identified (8, 9).

GBM consists of diverse cell populations that can differ in their tumor-promoting potential (10). Poorly differentiated (stem cell-like) GBM cells can be isolated from patient tumors and expanded for their use in chemical screens and diverse biological investigations using serum-free culture conditions as well as orthotopic xenografts in immunodeficient mice (10–14). Molecular pathways promoting GBM 'stemness' have been implicated in tumor development and phenotypic and molecular similarities between neural stem cells and poorly differentiated GBM cells have been described (10, 15, 16). In this context, the question arises as to whether chemical compounds that induce neural stem cell differentiation may also have a potential for reducing GBM growth.

KHS101 is one such compound that crosses the blood brain barrier (BBB) and selectively induces neuronal differentiation of hippocampal neural progenitor cells in vitro and in vivo (17). Previous studies have revealed transforming acidic coiled-coil containing protein 3 (TACC3) as a biologically relevant target of KHS101 (17, 18). TACC3 is a known regulator of cell division (19), and an emerging factor in GBM and tumor biology (20–22). The TACC3-targeting and

neural differentiation-promoting features of KHS101 prompted us to investigate the compound in human stem cell-like GBM cell models.

As inter- and intratumor heterogeneity is a major impediment to broadly efficacious GBM therapy, we also sought to address whether KHS101 would affect a spectrum of clinically-relevant GBM subtypes. To achieve this, we established a panel of different patient-derived primary and recurrent GBM cell models that were characterized through cytogenetic and single cell gene expression analysis. We observed that KHS101 induces a rapid and selective cytotoxic response in this heterogeneous spectrum of patient-derived GBM cell lines. Accordingly, we sought to identify the mechanisms of action behind the KHS101 anti-GBM activity utilizing gene expression analysis, affinity-based target identification, orthogonal chemical validation, and quantitative proteomics. These investigations were complemented by the analysis of energy metabolism and mitochondrial dynamics, which have been previously implicated in cancer biology and the regulation of cancer stem cell phenotypes (23–25). Furthermore, we investigated the KHS101 anti-GBM activity in established patient-derived tumor xenografts upon systemic administration.

Results

KHS101 selectively induces cytotoxicity in transcriptionally heterogeneous patient-derived GBM cell lines, independent of their molecular subtypes

GBM is characterized by intra- and intertumor heterogeneity that may hinder therapeutic success (26–28). To represent this molecular heterogeneity, we established six patient-derived tumor cell models from primary GBM (GBM1, 4, 13), recurrent GBM (GBM20), and rare GBM subtypes such as gliosarcoma (GBM11) and recurrent giant cell GBM (GBM14) (table S1). We hypothesized that single cell quantitative reverse transcription polymerase chain reaction (qRT-PCR) analysis using a selection of 85 classifier genes from the published proneural, neural, classical, and mesenchymal GBM molecular subtypes (28), and an additional selection of genes playing roles in GBM 'stemness' and proliferation, and the cell cycle, could indicate the molecular subtype heterogeneity within our GBM cell lines. Transcriptome profiling was carried out (after microfluidic chip-based capture of individual cells) by single cell qRT-PCR of ~45 randomly selected cells from each tumor model, and from the non-cancerous adult brain progenitor cell line NP1 (derivation is described in (14)). Based on the expression of the

aforementioned classifier genes, principal component analysis (PCA) indicated transcriptional heterogeneity between the different GBM (and NP1) cell lines, and between individual cells within each model (Fig. 1A and file S1). Using Computational analysis by cell cycle normalization, data discretization, and supervised classification, we stratified our cell lines based on their single cell transcriptional phenotypes (file S1). Our analysis showed that the GBM cell lines used here possessed either single (mesenchymal or proneural) or double (classical/proneural, mesenchymal/proneural) GBM subtype signatures (Fig. 1B and file S1).

To evaluate the role of KHS101 in tumor cell proliferation, we treated three GBM cell lines harboring different molecular signatures with 7.5 μM of KHS101 for 120 hours and assessed cell growth by real time imaging. Independent of classical, proneural, and mesenchymal molecular subtypes, KHS101 markedly attenuated tumor cell growth as compared to the cells treated with the vehicle (Dimethilsulfoxyde, DMSO). KHS101 did not affect cell proliferation in the non-cancerous NP1 cell line (Fig. 1C). We then evaluated KHS101in all 6 GBM cell lines and showed that KSH101 exhibited dose-dependent cytotoxic properties in all patient-derived GBM cell models, and also in the U251 and U87 GBM cell lines (Fig. 1D and fig. S1A). Neither bone morphogenetic protein 4 (BMP4)-induced differentiation of GBM cells (29) nor reduced oxygen tension (5% O_2) (30) interfered with KHS101-induced cytotoxicity, and NP cells were refractory to KHS101 treatment under both 21% and 5% O_2 conditions (fig. S1B).

KHS101 promotes autophagy and apoptosis in GBM cells

To examine the distinct cellular phenotypes of KHS101-treated GBM and NP cells, we carried out electron microscopy (EM) and immunocytochemistry-based imaging 12 hours after KHS101 (7.5 μM) addition to the GBM cell cultures. KHS101-treated GBM1 cells displayed a pronounced development of intracellular vacuoles compared to NP1 cells and to GBM cells treated with the vehicle (Fig. 2A top). Concomitantly, Microtubule-associated proteins 1A/1B light chain 3B (LC3B)-positive autophagosomal compartments increased in GBM1, and all other tested GBM cell models compared to the NP1 line (Fig. 2, A and B). The KHS101-induced macro-autophagy phenotype, measured as LC3B-stained cytoplasmic area, was concentration-dependent in 3 different GBM cell cultures tested (GBM1, GBM11, and GBM20), and was not detected in NP1 cells after a 12-hour treatment period (Fig. 2C). The effect of KHS101 on GBM autophagic flux was further confirmed by cellular accumulation of the cationic amphiphilic tracer dye CYTO-ID in the GBM1 cell line (Fig. 2D). Consistently, EM imaging indicated the

degradation of electron-dense cytoplasmic cellular content (Fig. S1D). The KHS101-induced autophagic phenotype was accompanied by a pro-apoptotic cell fate shown by marked increase in caspase 3/7 activation (luminescent assay) in the GBM1, GBM11, and GBM20 cell lines after a 48-hour treatment period (compared with the NP1 model; Fig. 2, E and F). A significant accumulation of Annexin V-positive apoptotic cells was also observed in GBM1 cells 48 hours after KHS101 treatment (fig. S1E). However, chemical inhibition of late-stage autophagy using bafilomycin A1 did not prevent this KHS101-induced apoptotic cell death (fig. S1E), suggesting that the latter is not autophagy-dependent.

KHS101 selectively disrupts metabolic pathways in GBM cells

TACC3 is a known target of KHS101 in rodent neural progenitor cells (17). KHS101 has been shown to cause cellular destabilization of TACC3, hence reducing endogenous TACC3 protein levels over time (18). Western blot analysis showed that KHS101 did not reduce TACC3 expression by >20% after a 12-hour treatment period in GBM1 cells; however, TACC3 appeared reduced by >40% from 18 hours onwards (fig S2A). Accordingly, KHS101-mediated TACC3 reduction was not linked to the rapid increase in autophagy marker positivity (from <10 to >80% CYTO-ID positive cells) measured over a treatment period of 12 hours in GBM1 cells treated with 7.5 μM of KHS101 (Fig. 3A). Consistently, the appearance of GBM cell vacuoles was observed ~4 hours after KHS101 addition by time lapse microscopy (movie S1). The KHS101-induced increased autophagy was not seen in TACC3 knockdown cells (fig. S2, B and C), hence excluding TACC3 downregulation as a critical player in mediating KHS101 cytotoxicity in the GBM context. Microarray transcriptome profiling (ArrayExpress, accession E-MTAB-5713) and gene enrichment analysis of KHS101-treated GBM1 cells (using the hypergeometric distribution) indicated that, in addition to differentially-regulated cell cycle pathways (Fig. 3B, left), genes associated with oxidative phosphorylation (OXPHOS) and the tricarboxylic acid (TCA) cycle were significantly modulated by KHS101 treatment ($P<4 \times 10^{-8}$; Fig. 3B and fig. S3A). The KHS101 effect on metabolism-related gene expression was observed using a selection of 25 differentially-expressed (>2-fold) marker mRNAs indicating alterations in glycolytic (Hexokinase 2, HK2 (31, 32)), oxidative (Heme Oxygenase 1, HMOX1 (33), and pro-apoptotic (Harakiri, BCL2 Interacting Protein, HRK (34)) pathways as well as downregulation of known GBM 'stemness' markers (Nitric Oxide Synthase 2, NOS2 (15), Inhibitor Of DNA Binding 1, HLH Protein, ID1 (35), and Oligodendrocyte Transcription Factor 2, OLIG2 (36) (Fig. 3B,

right). This KHS101-induced gene signature was confirmed by qRT-PCR in both primary (GBM1) and recurrent (GBM20) tumor models but was neither observed in KHS101-treated NP1 cells nor untreated TACC3-knockdown GBM1 cells (Fig. 3C).

To investigate whether the observed changes in metabolic gene expression were linked to a direct effect of KHS101 on GBM cell metabolism and mitochondrial function, metabolic phenotyping was carried out using five different GBM cell models, the NP1 and NP2 lines, and Normal (non-transformed) Human Astrocytes (NHA) using protocols described in (37). Extracellular flux analysis was carried out upon addition of vehicle or KHS101 and a metabolic phenogram was obtained by plotting the basal oxygen consumption rates (OCR; indicative of OXPHOS/mitochondrial respiration) of the different cell models as a function of their basal extracellular acidification rates (ECAR; an approximation of glycolytic activity). In contrast to the NP1, NP2, and NHA cell lines, the GBM cell lines exhibited elevated OCR and/or ECAR corresponding to 'aerobic' (GBM20), 'aerobic/energetic' (GBM1, GBM13), and 'energetic' (GBM11, GBM14) baseline phenotypes (Fig. 3D). Upon acute KHS101 treatment, the non-cancerous control cells remained within a 'modest' energetic phenotype window and exhibited a moderate increase in glycolytic activity ($\leq$ 2-fold; P=0.05). In contrast, KHS101 induced a significant hypoxic shift (P<0.0001; student's t-test, two tailed) and switch in metabolic baseline phenotype across all tested GBM cell models, independent of their molecular subtypes (Fig. 3D).

KHS101 affects glycolysis and the TCA cycle in GBM cells

Next, we examined intracellular fractional enrichment of glucose-derived carbon through glycolysis and the TCA cycle in the GBM1 and NP1 cell models using stable isotope substrate labeling with U-13C glucose (38) (fig. S4). Four hours after addition of KHS101 (7.5 μM), ^{13}C label enrichment was not significantly different for glucose (Fig. 4A) or fructose 6 phosphate (Fig. 4B). However we found a selective impairment of glycolysis in GBM1 compared with NP1 cells as indicated by the differential ^{13}C label enrichment of dihydroxyacetone phosphate (DHAP; Fig. 4C), glyceraldehyde 3-phosphate (GAP; Fig. 4D), glycerol 3-phosphate (G3P; Fig. 4E), phosphoenolpyruvate (PEP; Fig. 4F) and lactate (Fig. 4G). An unlabeled metabolite is detected as the molecular ion (M0) in the mass spectrum. Each additional ^{13}C-carbon atom introduced to the specific molecule gives rise to an increase in mass of 1 (M1, M2, M3, and so forth). The incorporation of the ^{13}C-label into the M2 isotopologues of TCA cycle intermediates

citrate (Fig. 4H), succinate (Fig. 4I), and malate (Fig. 4K) significantly decreased in KHS101-treated GBM1 cells ($P<0.05$), whereas enrichment of these metabolites remained unchanged in NP1 cells, indicating a selective perturbation of label enrichment through glycolysis and pyruvate dehydrogenase-initiated TCA cycle reactions. After 24 hours of KHS101 treatment, total cellular adenosine triphosphate (ATP) levels were reduced (≥50%) in GBM1 compared with NP1 cells (fig. S3B). In addition, we noted a higher fractional enrichment of the M1 isotopologues of citrate (Fig. 4H), succinate (Fig. 4I), fumarate (Fig 4J) and malate (Fig 4K) in control GBM versus NP1 cells, which was selectively reduced by KHS101 in GBM1 cells. Relative enrichment of the M3 isotopologues of TCA cycle intermediates was elevated in GBM1 versus NP1 cells (Fig. 4 H, I, J, and K). Increased labelling of M3 aspartate (a proxy for oxaloacetate), through the action of pyruvate carboxylase, was observed in KHS101-treated GBM cells (Fig 4L). In summary, these findings indicate that KHS101 selectively impairs aerobic glycolysis, mitochondrial respiration-dependent, and malic enzyme-dependent biosynthetic pathways in GBM cells.

KHS101 interacts with HSPD1 in GBM cells

Mitochondrial dynamics are important mediators of tumorigenesis and cancer stem cell phenotypes (23, 25). To elucidate the cellular target(s) underlying the reduced mitochondrial and metabolic capacity in KHS101-treated GBM cells, we investigated the physical interaction of KHS101 with potential cellular protein(s) using an established affinity-based target identification protocol (17). The photoaffinity probe KHS101-BP (a KHS101 derivative containing a benzophenone moiety and an alkyne substituent) and KHS101 showed similar bioactivity in GBM cells (fig. S5). A distinct KHS101-BP-protein complex of ~60 kDa (isoelectric point ~5.7) appeared reduced by >50% in presence of a 50-fold excess of unlabeled KHS101, and was therefore used for examination of KHS101-interacting protein (Fig. 5A). Proteomics analysis revealed that the KHS101-BP-bound protein corresponded to the mitochondrial 60 kDa heat shock protein 1 (HSPD1).

A specific interaction between KHS101 and HSPD1 was further observed by in vitro pull-down experiments using human recombinant HSPD1 protein (Fig. 5B). Cellular fractionation followed by Western blot analysis showed that HSPD1 was overexpressed in GBM1 cells and predominantly localized to the mitochondria as indicated by a marked increase

in the mitochondrial to cytoplasmic ratio compared with NP1 cells ($P<0.01$; Fig. 5C). Reduction of HSPD1 expression by lentiviral short hairpin (sh)RNA in GBM1 cells by 50-65% ($P<0.01$; fig. S6A) was associated with an increase in mRNA expression of stress-inducible chaperone Heat Shock Protein Family A (Hsp70) Member 1A (HSPA1A; >5-fold; $P<0.05$), which has been linked to mitochondrial proteostasis in cancer cells (fig. S6B) (39). In agreement with a reported role for HSPD1 in glioma cell line proliferation (40), a decline in mitochondrial activity/OXPHOS (~50%; fig. S6C), and a significant decrease in proliferation (~50%, $P<0.0001$), was observed in the HSPD1 shRNA-harboring (low HSPD1-expressing) GBM1 cells (fig. S6D; note that KHS101 addition further reduced the growth of HSPD1 knockdown GBM1 cells). KHS101 altered neither HSPD1 protein levels nor HSPD1 mRNA expression (Fig. 5D, and E, and fig. S6E), suggesting that the KHS101-GBM cytotoxicity is independent of HSPD1 mRNA/protein downregulation.

KHS101 aggregates HSPD1 and metabolic enzymes in GBM cells promoting their metabolic exhaustion

To investigate whether KHS101 directly inhibits HSPD1 function, HSPD1/Heat Shock Protein Family E (Hsp10) Member 1 (HSPE1) chaperonin complex activity was assessed upon KHS101 addition in vitro. A concentration-dependent inhibition of HSPD1-dependent substrate re-folding was readily detected in presence of KHS101 ($IC50=14.4\ \mu M$) (Fig. 6A). Re-folding activity remained unaffected upon addition of a structurally closely related KHS101 analog (HB072; Fig. 6B, file S3), which was phenotypically-inactive in GBM cells (fig. S7A). In contrast, the mitochondrial HSPD1-targeting natural product myrtucommulone (MC (41)) elicited a concentration dependent decrease in HSPD1/HSPE1 re-folding activity (Fig. 6B). Moreover, MC and KHS101 shared mitochondrial and bioenergetic stress-promoting activities as observed by reduced mitochondrial respiration capacity, upregulation of DNA Damage Inducible Transcript 3 (DDIT3) and HMOX1 mRNA, and ATP depletion (fig. S7, B to D). Consistently, MC recapitulated the KHS101-induced autophagy and cell death phenotype in GBM cells (fig. S7, E and F).

We next asked whether KHS101 disrupts mitochondrial HSPD1 function in a cell-based in vitro system. To this end, we quantified protein aggregation by fractionation of detergent-insoluble mitochondrial proteins in GBM1 compared with NP1 cells upon compound addition.

Silver staining indicated that aggregated proteins (pellet) were enriched by ~4-fold ($P<0.01$), whereas soluble protein enrichment was not significantly affected in GBM1 compared with NP1 cells 1 hour after KHS101 treatment (Fig. 6C). Proteomics analysis determined that HSPD1 and enzymes with functions in glycolysis (Aldolase, Fructose-Bisphosphate A, ALDOA), TCA cycle (Dihydrolipoyllysine-residue succinyltransferase component of 2-oxoglutarate dehydrogenase complex, DLST), OXPHOS (ATP Synthase F1 Subunit Alpha, ATP5A1), and mitochondrial integrity (Lon Peptidase 1, Mitochondrial, LONP1 (42)) were specifically enriched in the aggregated protein fractions of GBM1 compared to NP1 cells (table S2). Consistently, the aggregated proteins readily integrated into a predicted HSPD1-centered protein-protein interaction network using the Search Tool for the Retrieval of Interacting Genes/Proteins (STRING; (43); Fig. 6D). In addition to mitochondrial fractionation, a quantitative global proteomics analysis of KHS101-treated GBM1 cells (data deposited at the PRoteomics IDEntifications (PRIDE) database , identifier PXD009429) showed that the following aggregated proteins of the predicted HSPD1 interaction network were significantly downregulated 1-hour after KHS101 treatment ($P<7.5 \times 10^{-7}$): DLST, ATP5A1, Solute Carrier Family 25 Member 3 (SLC25A3), ALDOA, Pyruvate Kinase M1/2 (PKM2), Phosphoenolpyruvate Carboxykinase 2, Mitochondrial (PCK2), Serine Hydroxymethyltransferase 2 (SHMT2), Phosphoglycerate Dehydrogenase (PHGDH), HSPD1, Heat Shock Protein 90 Alpha Family Class B Member 1 (HSP90AB1), and LONP1 (Fig. 6E and file S3). Changes in the KHS101-regulated GBM proteome were time-dependent as indicated by PCA and differential peptide abundances (fig. S8, A and B). Global protein abundance was decreased by KHS101 at both the 1-hour and 12-hour time points. Compared with t_0, 9500 and 9607 polypeptides were significantly downregulated ($P \leq 0.05$), whereas only 93 and 16 proteins were markedly upregulated at the 1- and 12-hour time points, respectively (Fig. 6E and fig. S8C, and file S3). Protein set enrichment analysis indicated that mitochondrial rather than endoplasmic reticulum (ER) pathways were affected (Fig. 6E, fig. S8C, file S3). In summary, these findings corroborate a link between the KHS101-mediated disruption of mitochondrial HSPD1 activity and metabolic stress in GBM cells.

KHS101 attenuates tumor growth and invasion in vivo

To investigate the potential pharmacological effects of KHS101 on GBM in vivo, xenograft tumors were allowed to establish for 6 weeks after injection of GBM1 cells (1×10^5

cells) into the forebrain striatum and treated with vehicle or KHS101 for 10 days (s.c., 6 mg/kg, twice daily). Subsequently, Nicotinamide adenine dinucleotide (NADH)/Nicotinamide adenine dinucleotide phosphate (NAD(P)H) and Flavin adenine dinucleotide (FAD) autofluorescence (AF; fig. S9A) was examined as an indicator of metabolic and mitochondrial activity in situ (44). Analysis of tumor tissue sections showed that the AF signal area was predominantly cytoplasmic and significantly upregulated after systemic delivery of KHS101 compared with the vehicle control ($P<0.01$; Fig. 7A and fig. S9, A and B). Consistently, fluorescence-lifetime imaging microscopy (FLIM) revealed an elevated cytoplasmic fluorescence (corresponding to free NAD(P)H)) 1 hour after KHS101 addition in cultured GBM1 cells (fig. S9C).

To examine whether the observed mitochondrial/redox anomaly was associated with reduced tumor progression, we adapted the KHS101 dosing regimen from previous neurogenesis work in rats (17) using a 10-week tumor treatment strategy (s.c., 6 mg/kg, twice a day, and bi-weekly treatment alternating five and three treatment days per week). Immunohistological analysis of the vehicle (V)- and KHS101 (K)-treated tumors at the 16-week endpoint showed an increase in HK2-positive tumor area in KHS-treated tumors (Fig. 7B and fig. S10A), which was in line with the KHS101-induced increase in HK2 mRNA in GBM cell cultures. Concomitantly, tumor cell proliferation was markedly reduced in KHS101-treated tumors (~2-fold) as assessed by MKI67 staining (Fig. 7B and fig. S10A). This finding was consistent with a homogenous decrease in MKI67 expression and abrogation of clonal growth capacity in individually profiled GBM1 cells in vitro (Fig. 7, C and D). KHS101-treated tumors showed signs of elevated cell death (reduced cellularity/increased pyknosis) compared with tumors treated with vehicle control (Fig. 7E and fig. S10B). The highly invasive phenotype of the GBM1 xenograft tumor model (14) enabled quantification of caudal tumor expansion and tumor cell migration across the corpus callosum into the contralateral hemisphere (a pathological hallmark of advanced GBM). KHS101 treatment markedly reduced both frontal-to-caudal tumor expansion (Fig. 7F), and corpus callosum invasion of Vimentin-positive GBM1 cells ($\geq$2-fold) (Fig. 7G). Histological analysis demonstrated preserved hepatic architecture in KHS101-treated animals (fig. S10C).

KHS101 treatment increases survival of xenograft tumor-bearing mice

Consistent with the notion of a pro-tumorigenic effect of elevated HSPD1 (45), exploration of the REpository of Molecular BRAin Neoplasia DaTa set (REMBRANDT (46);

http://www.betastasis.com/glioma/rembrandt/) suggested thatHSPD1 mRNA expression negatively correlated with glioma survival (Fig. 8A). Accordingly, we further investigated whether KHS101 prolonged survival in a xenograft model of GBM. To this end, we used a giant cell GBM-based model, established with exclusively in vivo-propagated primary cells (GBMX1; onset of morbidity: 10-13 weeks). We found that the survival of animals carrying GBMX1-tumors (established 2 or 6 weeks before treatment) was markedly increased by the KHS101 treatment regimen for 10 weeks (Fig. 8B). None of the mice had to be removed from the study due to adverse side effects of the treatment. An additional experiment using a continuous KHS101 treatment regime until the experimental endpoints, also showed a marked increase in the survival of GBMX1-bearing animals (Fig. 8C). Histological endpoint analysis of KHS101- and vehicle-treated animals confirmed a significantly decreased tumor size in KHS101-treated mice (~2-fold, $P<0.01$; Fig. 8D). In summary, these results indicate significant anti-GBM effects of KHS101 in vivo, without discernible adverse toxicity.

Discussion

GBM is a devastating cancer with limited treatment options and correspondingly poor patient outcomes. We began our investigation with the hypothesis that GBM tumor stem cell-like cells might be eradicated by a small molecule-mediated pro-differentiation phenotype (12). In this context, the compound KHS101 shows BBB penetrability as well as non-toxic neuronal differentiation properties by targeting TACC3 (17, 47). However, instead of a 'forced' pro-differentiation phenotype that reduces GBM tumorigenicity in a cell death-independent manner (14, 29), we observed a cytotoxic lethal GBM cell fate, characterized by autophagy-driven cellular self-destruction.

One challenge for GBM target discovery and validation is to incorporate the ever-changing composition of molecularly and phenotypically diverse tumor cell populations (26, 27, 48) into preclinical disease modeling. To this end, transcriptional diversity among and within our six patient-derived models was revealed by microfluidic single cell qRT-PCR analysis. We adapted computational approaches that robustly indicated classical, proneural, and mesenchymal GBM subtype compartments in our GBM models, that were independent of GBM subtype features, pro-differentiation signaling (14, 29), low oxygen culture conditions, and parental tumor origin (primary versus recurrent GBM, and MGMT methylation status).

Consistent with previous work (18), KHS101 treatment decreased endogenous TACC3 protein in GBM cells over time. The resulting TACC3 degradation kinetics (onset ≥18 hours) was not involved in the more rapidly-evolving autophagy and cytoplasmic degradation processes in GBM cells. However, the KHS101-mediated decrease in TACC3 levels may have contributed to the alterations in GBM cell cycle and mitotic pathways as indicated by microarray gene expression analysis 24 hours after KHS101 addition. KHS101-induced gene expression changes (observed for SLC2A1, HK2, HMOX1, and DDIT3) suggested a yet unexplored KHS101 bioactivity in regards to metabolic and mitochondrial pathway perturbation. Consistent with the notion that altered energy metabolism is a hallmark of cancers and a potential tumor cell vulnerability (24), the GBM cell models persistently exhibited elevated bioenergetic demands compared with NP and astrocyte cell lines. Both intracellular and extracellular metabolic phenotyping indicated that KHS101 disrupted GBM cell energy metabolism. Glucose transporter gene expression (SLC2A1 and SLC2A3) was increased in GBM cells after a 24-hour treatment period. Moreover, HK2 expression increased after KHS101 treatment in vitro and in vivo. HK2 is a key enzyme for enhanced glucose turnover that depends on ATP availability (32), which was reduced in KHS101-treated GBM cells at the 24-hour time point. Fractional enrichment of glucose-derived carbon through glycolysis and the TCA cycle was impaired in the GBM cells and the latter was indicated by a reduction in ^{13}C-label incorporation into the M2 isotopologues of TCA cycle intermediates. The M1 isotopologues of TCA cycle intermediates were likely derived from the generation of M1-labelled pyruvate, by the action of malic enzyme 1 (ME1), which subsequently re-enters the TCA cycle either by the action of pyruvate carboxylase or the reverse ME1 reaction. ME1 is overexpressed in cancer cells to meet redox balancing and lipid biosynthetic demands, and its inhibition has been suggested to impair cancer cell growth (49). Increased labeling of M3 aspartate (a proxy for oxaloacetate) may represent a compensatory carbon entry into the TCA cycle in KHS101-treated GBM cells via increased, pyruvate carboxylase-mediated, pyruvate anaplerosis, which has previously been described in lung metastases (50). Consistent with bioenergetic changes, stress response genes (DDIT3 and HMOX1 indicating mitochondrial stress in glioma depending on the experimental context (51, 52)) were upregulated by KHS101. Moreover, a NAD(P)H cytoplasmic accumulation (indicating mitochondrial/redox anomalies (44, 53)) was observed in GBM cells and xenograft tumors upon KHS101 treatment. It is plausible that, concomitant with KHS101-induced advances in

bioenergetic insufficiencies, cellular stress evolved and spread across the GBM cell organelle system, for example via the mitochondrial unfolded protein response (as indicated by the upregulation of DDIT3 and TRIB3 mRNA expression in treated GBM1 cells; (54, 55)).

In agreement with a KHS101 interference with mitochondrial dynamics, affinity-based target identification suggested a physical interaction between KHS101 and the mitochondrial chaperone HSPD1 in GBM cells. The reduction of HSPD1 using shRNAs expectedly affected GBM cell growth and mitochondrial capacity (40), and a potential compensation for reduced HSPD1 expression via HSPA1A mRNA upregulation was observed. However, KHS101 did not affect cellular HSPD1 mRNA and protein levels, highlighting the importance of recognizing differences between genetic and small-molecule target inhibition (reviewed in (56)). As affinity-based target identification provides important, but not sufficient, evidence for small molecule mechanisms of action investigations (9), we sought to address whether KHS101 disrupted HSPD1 function. The activity of the HSPD1/HSPE1 complex was reduced by KHS101 in a concentration-dependent fashion in vitro. A structurally-related KHS101 analog that did not affect HSPD1/HSPE1 chaperone activity (HB072), remained phenotypically-inactive in GBM cells. In contrast, a structurally-unrelated positive control for mitochondrial HSPD1 inhibition ((MC; (57)), fully recapitulated the KHS101-induced GBM cell cytotoxicity.

A selective aggregation of HSPD1 and its potential client proteins was observed in GBM cells 1 hour after KHS101 addition. The acute deregulation of a predicted HSPD1-centered enzymatic network, including ALDOA (regulating glycolysis), DLST (regulating TCA cycle), ATP5A1 (regulating OXPHOS), and the chaperone LONP1 (regulating mitochondrial integrity in cancer cells (42) provides an explanation for the rapidly-evolving metabolic stress that was not uniquely mitochondrial. Mitochondrial fractionation of aggregated ALDOA and PKM2 proteins suggests close association of these enzymes with GBM cell mitochondria, a phenomenon reported for HK2 in the cancer cell context (32).

Selective effects of KHS101 towards brain cancer cells were observed throughout our study at protein, metabolite, mRNA, and organelle levels. Cellular self-degradation processes were markedly pronounced in GBM but not NP cells 12 hours after KHS101 treatment. The loss of stem cell-like features and the significant increase in apoptotic cell death over time (>24 hours) indicates that GBM cells failed to compensate for the KHS101-mediated impairment of critical metabolic and mitochondrial fitness and ATP production. Taken together, these results

support a causative relationship between the KHS101-induced HSPD1 disruption and a lethal GBM cellular phenotype.

KHS101 activity has not been associated with toxicity in non-cancer contexts in vitro and in vivo (17, 18, 47, 58). KHS101 showed favorable in vivo properties including accelerated neuronal differentiation in adult rats (without affecting apoptosis of brain cells (17, 47)). Consistent with the specific KHS101 cytotoxicity in GBM compared with NP cells, the compound markedly decreased the progression of established xenograft tumors, whereas adverse effects (liver toxicity) were not observed in mice after prolonged (10-week) systemic administration.

There are some limitations to our study. KHS101 is an experimental/preclinical compound that may require chemical and pharmacological optimization before KHS101-like bioactivities can be tested in clinical applications. The exact molecular nature of the KHS101-HSPD1 interaction, and the role of HSPD1 in the metabolic reprogramming that drives brain tumorigenesis remain to be further investigated.

In summary, this experimental small molecule phenotype and target profiling study identifies HSPD1 enzymatic function as a specific molecular vulnerability linked to energy metabolism in GBM cell models. A lethal GBM cell fate can be selectively triggered in a heterogeneous spectrum of GBM cells by a single agent. These findings highlight the potential for using KHS101-like compounds for therapeutic developments.

Materials and Methods

Study design

Our objective was to characterize the effect of the synthetic small molecule KHS101 in the GBM cellular context in vitro and in vivo. The control and treatment groups and the number of biological replicates (sample sizes) for each experiment are specified in the figure legends. For in vivo tumor xenograft studies, no power analysis was performed to predetermine the sample size, animals were randomly allocated to the control and treatment groups and housed together to minimize environmental differences and experimental bias. Analysis of endpoint readouts were carried out in a blinded fashion.

Statistical analysis

A minimum of 3 independent biological repeats were analyzed using the student's t-test (two tailed, equal variance), One-way or two-way ANOVA (Tukey post-hoc), or Benjamini-Hochberg procedure (for false discovery rates) as specified in the figure legends. Data were expressed as mean ± SD. One biological repeat comprised a minimum of 3 technical replicates. Approximate normal distribution of data was assumed. For xenograft tumor analysis, the Mann-Whitney U-test was used (one tailed). For Kaplan-Meier xenograft tumor analysis, the significance was calculated using the log-rank test.

For all other Materials and Methods, see Supplementary Materials.

List of Supplementary Materials

Fig. S1. KHS101 reduces GBM cell viability in different culture conditions.

Fig. S2. TACC3 downregulation is not causally linked to KHS101-induced GBM cell degradation.

Fig. S3. KHS101 disrupts ATP production in GBM cells.

Fig. S4. Schematic representation of glucose carbon tracing through glycolysis, the TCA cycle, malic enzyme and pyruvate carboxylase reactions.

Fig. S5. KHS101-BP and KHS101 show comparable bioactivities in GBM cells.

Fig. S6. RNAi-mediated knockdown of HSPD1 results in reduced oxidative capacity and proliferation in GBM cells.

Fig. S7. MC recapitulates KHS101 cytotoxicity in GBM cells.

Fig. S8. Time-dependent changes in protein abundances in KHS101-treated GBM1 cells.Fig. S9. KHS101 induces NAD(P)H/NAD+ imbalance in GBM1 cells and xenograft tumors.

Fig. S9. Anti-tumor effects of KHS101 in xenograft tumor experiments.

Fig. S10. Comparison of HSPD1 mRNA expression levels within the indicated brain tumor and control (non-cancer) categories using the 'REMBRANDT' data set

Table S1. Overview of patient-derived GBM cell model characterization.

Table S2. List of aggregated proteins (and their known functions) that were identified within the mitochondrial fraction of KHS101-treated GBM1 cells.

Table S3. List of Delta-gene assays (Fluidigm) used for single cell qRT-PCR analysis.

Table S4. Chemical structures of the indicated compounds.

Table S5. List of Delta-gene assays (Fluidigm) used for single cell qRT-PCR analysis.

Additional Materials and Methods.

File S1. A report of the bioinformatics (R) analysis utilizing single cell gene expression data.

File S2. Study data in tabular format and organized by figure.

File S3. Supplementary lists of up- and down-regulated proteins

File S4. A description of chemical synthesis and compound characterization.

Movie S1. Live cell imaging of GBM1 cells comparing DMSO (0.1%, left panel) with KHS101 treatment (7.5 μM, right panel). Timeline as indicated.

References:

1. M. Preusser et al., Current concepts and management of glioblastoma. Ann. Neurol. **70**, 9–21 (2011).

2. S. K. Carlsson, S. P. Brothers, C. Wahlestedt, Emerging treatment strategies for glioblastoma multiforme. EMBO Mol. Med. **6**, 1359–1370 (2014).

3. D. G. Trembath, A. Lal, D. J. Kroll, N. H. Oberlies, G. J. Riggins, A novel small molecule that selectively inhibits glioblastoma cells expressing EGFRvIII. Mol. Cancer. **6**, 30 (2007).

4. Z. Cheng et al., Inhibition of BET bromodomain targets genetically diverse glioblastoma. Clin. Cancer Res. **19**, 1748–1759 (2013).

5. A. De Robertis et al., Identification and characterization of a small-molecule inhibitor of Wnt signaling in glioblastoma cells. Mol. Cancer Ther. **12**, 1180–1189 (2013).

6. K. Shchors, A. Massaras, D. Hanahan, Dual Targeting of the Autophagic Regulatory Circuitry in Gliomas with Repurposed Drugs Elicits Cell-Lethal Autophagy and Therapeutic Benefit. Cancer Cell. **28**, 456–471 (2015).

7. M. Gallo et al., MLL5 Orchestrates a Cancer Self-Renewal State by Repressing the Histone Variant H3.3 and Globally Reorganizing Chromatin. Cancer Cell. **28**, 715–729 (2015).

8. J. G. Moffat, F. Vincent, J. A. Lee, J. Eder, M. Prunotto, Opportunities and challenges in phenotypic drug discovery: an industry perspective. Nat. Rev. Drug Discov. **16**, 531–543 (2017).

9. B. K. Wagner, S. L. Schreiber, The Power of Sophisticated Phenotypic Screening and Modern Mechanism-of-Action Methods. Cell Chem. Biol. **23**, 3–9 (2016).

10. P. B. Dirks, Brain tumor stem cells: the cancer stem cell hypothesis writ large. Mol. Oncol. **4**, 420–430 (2010).

11. J. Lee et al., Tumor stem cells derived from glioblastomas cultured in bFGF and EGF more closely mirror the phenotype and genotype of primary tumors than do serum-cultured cell lines. Cancer Cell. **9**, 391–403 (2006).

12. H. Wurdak, Exploring the cancer stem cell phenotype with high-throughput screening applications. Future Med. Chem. **4**, 1229–1241 (2012).

13. S. M. Pollard et al., Glioma stem cell lines expanded in adherent culture have tumor-specific phenotypes and are suitable for chemical and genetic screens. Cell Stem Cell. **4**, 568–580 (2009).

14. H. Wurdak et al., An RNAi screen identifies TRRAP as a regulator of brain tumor-initiating cell differentiation. Cell Stem Cell. **6**, 37–47 (2010).

15. C. E. Eyler et al., Glioma stem cell proliferation and tumor growth are promoted by nitric oxide synthase-2. Cell. **146**, 53–66 (2011).

16. J. D. Lathia, S. C. Mack, E. E. Mulkearns-Hubert, C. L. L. Valentim, J. N. Rich, Cancer stem cells in glioblastoma. Genes Dev. **29**, 1203–1217 (2015).

17. H. Wurdak et al., A small molecule accelerates neuronal differentiation in the adult rat. Proc Natl Acad Sci USA. **107**, 16542–16547 (2010).

18. Y. Guo et al., Regulating the ARNT/TACC3 axis: multiple approaches to manipulating protein/protein interactions with small molecules. ACS Chem. Biol. **8**, 626–635 (2013).

19. F. E. Hood, S. J. Royle, Pulling it together: The mitotic function of TACC3. Bioarchitecture. **1**, 105–109 (2011).

20. D. Singh et al., Transforming fusions of FGFR and TACC genes in human glioblastoma. Science. **337**, 1231–1235 (2012).

21. C. G. Duncan et al., Integrated genomic analyses identify ERRFI1 and TACC3 as glioblastoma-targeted genes. Oncotarget. **1**, 265–277 (2010).

22. R. Costa et al., FGFR3-TACC3 fusion in solid tumors: mini review. Oncotarget. **7**, 55924–55938 (2016).

23. S. Vyas, E. Zaganjor, M. C. Haigis, Mitochondria and Cancer. Cell. **166**, 555–566 (2016).

24. D. Hanahan, R. A. Weinberg, Hallmarks of cancer: the next generation. Cell. **144**, 646–674 (2011).

25. H. Chen, D. C. Chan, Mitochondrial dynamics in regulating the unique phenotypes of cancer and stem cells. Cell Metab. **26**, 39–48 (2017).

26. R. Bonavia, M.-M. Inda, W. K. Cavenee, F. B. Furnari, Heterogeneity maintenance in glioblastoma: a social network. Cancer Res. **71**, 4055–4060 (2011).

27. A. P. Patel et al., Single-cell RNA-seq highlights intratumoral heterogeneity in primary glioblastoma. Science. **344**, 1396–1401 (2014).

28. R. G. W. Verhaak et al., Integrated genomic analysis identifies clinically relevant subtypes of glioblastoma characterized by abnormalities in PDGFRA, IDH1, EGFR, and NF1. Cancer Cell. **17**, 98–110 (2010).

29. S. G. M. Piccirillo et al., Bone morphogenetic proteins inhibit the tumorigenic potential of human brain tumour-initiating cells. Nature. **444**, 761–765 (2006).

30. J. M. Heddleston et al., Glioma stem cell maintenance: the role of the microenvironment. Curr. Pharm. Des. **17**, 2386–2401 (2011).

31. L. Wang et al., Hexokinase 2-mediated Warburg effect is required for PTEN- and p53-deficiency-driven prostate cancer growth. Cell Rep. **8**, 1461–1474 (2014).

32. S. P. Mathupala, Y. H. Ko, P. L. Pedersen, Hexokinase II: cancer's double-edged sword acting as both facilitator and gatekeeper of malignancy when bound to mitochondria. Oncogene. **25**, 4777–4786 (2006).

33. C. Gorrini, I. S. Harris, T. W. Mak, Modulation of oxidative stress as an anticancer strategy. Nat. Rev. Drug Discov. **12**, 931–947 (2013).

34. M. Nakamura, K. Shimada, N. Konishi, The role of HRK gene in human cancer. Oncogene. **27 Suppl 1**, S105-13 (2008).

35. L. Soroceanu et al., Id-1 is a key transcriptional regulator of glioblastoma aggressiveness and a novel therapeutic target. Cancer Res. **73**, 1559–1569 (2013).

36. M. L. Suvà et al., Reconstructing and reprogramming the tumor-propagating potential of glioblastoma stem-like cells. Cell. **157**, 580–594 (2014).

37. L. S. Pike Winer, M. Wu, Rapid analysis of glycolytic and oxidative substrate flux of cancer cells in a microplate. PLoS ONE. **9**, e109916 (2014).

38. L. D. Roberts, S. Virtue, A. Vidal-Puig, A. W. Nicholls, J. L. Griffin, Metabolic phenotyping of a model of adipocyte differentiation. Physiol. Genomics. **39**, 109–119 (2009).

39. J. I.-J. Leu et al., Inhibition of stress-inducible HSP70 impairs mitochondrial proteostasis and function. Oncotarget. **8**, 45656–45669 (2017).

40. H. Tang et al., Down-regulation of HSP60 Suppresses the Proliferation of Glioblastoma Cells via the ROS/AMPK/mTOR Pathway. Sci. Rep. **6**, 28388 (2016).

41. K. Wiechmann et al., Mitochondrial Chaperonin HSP60 Is the Apoptosis-Related Target for Myrtucommulone. Cell Chem. Biol. **24**, 614–623.e6 (2017).

42. P. M. Quirós et al., ATP-dependent Lon protease controls tumor bioenergetics by reprogramming mitochondrial activity. Cell Rep. **8**, 542–556 (2014).

43. L. J. Jensen et al., STRING 8--a global view on proteins and their functional interactions in 630 organisms. Nucleic Acids Res. **37**, D412-6 (2009).

44. A. A. Heikal, Intracellular coenzymes as natural biomarkers for metabolic activities and mitochondrial anomalies. Biomark. Med. **4**, 241–263 (2010).

45. F. Cappello, E. Conway de Macario, L. Marasà, G. Zummo, A. J. L. Macario, Hsp60 expression, new locations, functions and perspectives for cancer diagnosis and therapy. Cancer Biol. Ther. **7**, 801–809 (2008).

46. S. Madhavan et al., Rembrandt: helping personalized medicine become a reality through integrative translational research. Mol. Cancer Res. **7**, 157–167 (2009).

47. Y. Zhang, C. Kibaly, C. Xu, H. H. Loh, P.-Y. Law, Temporal effect of manipulating NeuroD1 expression with the synthetic small molecule KHS101 on morphine contextual

memory. Neuropharmacology. **126**, 58–69 (2017).

48. F. Buettner et al., Computational analysis of cell-to-cell heterogeneity in single-cell RNA-sequencing data reveals hidden subpopulations of cells. Nat. Biotechnol. **33**, 155–160 (2015).

49. S. Murai et al., Inhibition of malic enzyme 1 disrupts cellular metabolism and leads to vulnerability in cancer cells in glucose-restricted conditions. Oncogenesis. **6**, e329 (2017).

50. S. Christen et al., Breast Cancer-Derived Lung Metastases Show Increased Pyruvate Carboxylase-Dependent Anaplerosis. Cell Rep. **17**, 837–848 (2016).

51. M. D. Siegelin et al., Exploiting the mitochondrial unfolded protein response for cancer therapy in mice and human cells. J. Clin. Invest. **121**, 1349–1360 (2011).

52. E. Singer et al., Reactive oxygen species-mediated therapeutic response and resistance in glioblastoma. Cell Death Dis. **6**, e1601 (2015).

53. T. S. Blacker, M. R. Duchen, Investigating mitochondrial redox state using NADH and NADPH autofluorescence. Free Radic. Biol. Med. **100**, 53–65 (2016).

54. N. Ohoka, S. Yoshii, T. Hattori, K. Onozaki, H. Hayashi, TRB3, a novel ER stress-inducible gene, is induced via ATF4-CHOP pathway and is involved in cell death. EMBO J. **24**, 1243–1255 (2005).

55. T. Shpilka, C. M. Haynes, The mitochondrial UPR: mechanisms, physiological functions and implications in ageing. Nat. Rev. Mol. Cell Biol. **19**, 109–120 (2018).

56. W. A. Weiss, S. S. Taylor, K. M. Shokat, Recognizing and exploiting differences between RNAi and small-molecule inhibitors. Nat. Chem. Biol. **3**, 739–744 (2007).

57. K. Wiechmann, H. Müller, D. Fischer, J. Jauch, O. Werz, The acylphloroglucinols hyperforin and myrtucommulone A cause mitochondrial dysfunctions in leukemic cells by direct interference with mitochondria. Apoptosis. **20**, 1508–1517 (2015).

58. M. Warashina et al., A synthetic small molecule that induces neuronal differentiation of adult hippocampal neural progenitor cells. Angew Chem Int Ed Engl. **45**, 591–593 (2006).

59. J. A. Vizcaíno et al., 2016 update of the PRIDE database and its related tools. Nucleic Acids Res. **44**, 11033 (2016).

60. O. Troyanskaya et al., Missing value estimation methods for DNA microarrays. Bioinformatics. **17**, 520–525 (2001).

Acknowledgments: S.J.A. and H.B.S.G. acknowledge PhD studentship support funds from the University of Huddersfield. We thank J. Jauch (Saarland University) for kindly providing myrtucommulone, S. Wilkinson for help with LC3/autophagy protocols, D. J. Beech for microscopy support and resources, P. Roberts and K. Rankeillor for help with cytogenetic analysis, P. O'Toole and M. Stark for help with EM imaging, H. Payne for help with qRT-PCR protocols, C. Simmons for assistance with chemical synthesis, and N. Riobo-Del Galdo, P. Ceppi, and P.J. Selby for useful discussions.

Funding: H.W. acknowledges support from the MRC New Investigator Award (MR/J001171/1), the Marie Curie European/International Reintegration Grant (303814), and Worldwide Cancer Research project grant (13-0146). J.W. and E.S.P. acknowledge support from Brain Tumor Research and Support across Yorkshire. R.K.M. acknowledges support from the Leeds Cancer Research UK-Centre Clinical Fellowship. H.A.B. acknowledges support from EPSRC (EP/M506552/1). S.C.S. acknowledges support from the Brain Tumour Charity (program grant 13/192). S.J.A. and H.B.S.G. acknowledge PhD studentship support funds from the University of Huddersfield. C.A. acknowledges support from Cancer Research UK (C48431/A18717; C37059/A1636CRUK).

Author contributions: E.S.P., V.B.K., C.A., B dS., A.N.H., E.C-B. J.W., H.B.S.G., H.S., A.J.D., L.D.R., S.J.A., and H.W. performed cell culture-based experimental work. A.P. performed single cell profiling. H.A.B. and R.S.B. performed chemical synthesis. E.S.P., H.A.B., H.S., R.S.B., and S.Z. carried out biochemical experiments. V.B.K., R.K.M., A.P., M.L., and H.W. conducted in vivo studies. E.S.P., V.B.K., C.A., E.M.R., B dS., A.N.H., S.B., E.C-B., H.B.S.G, H.S., A.D., L.D.R., R.S.B., S.J.A., S.Z., F.M., and H.W. carried out data analysis. E.M.R. and F.M. generated computer code. A.D., P.C., S.C.S. and HW managed data and provided materials. E.S.P., V.B.K, R.K.M., and H.W. prepared the manuscript and figures. J.E.G. R.S.B., S.J.A., S.Z., F.M., and H.W. provided project leadership.

Competing interests: C.A. is an author of patent applications WO2017181202A2 and WO2018083467A1, which are pending and relate to the use of circulating tumour DNA as a biomarker in lung cancer. S.D.is the director of AD Bioinformatics Ltd which provides

consultancy and data analysis to external companies (not employed for this study). S.C.S. has performed consultancy work for AbbVie pharmaceuticals (unrelated to this study). J.E.G. is a consultant for Daiichi Sankyo, Viewpoint Therapeutics and Tenaya Therapeutics (not employed for this study).

Data and materials availability: Gene expression microarray data that support the findings of this study have been deposited in ArrayExpress, accession E-MTAB-5713. The mass spectrometry proteomics data have been deposited to the ProteomeXchange Consortium via the PRIDE partner repository (59) with the dataset identifier PXD009429. The rest of the data associated with this study are present in the paper or supplementary materials.

Figure legends

Fig. 1. KHS101 exhibits cytotoxicity in molecularly-diverse GBM models. (**A**) Principle component analysis in individual cells within the patient-derived GBM and NP1 lines. (**B**) Radar plots depicting the GBM subtype compartments (classical (C), proneural (P), mesenchymal (M) and neural (N)) of the GBM1 (left), GBM11 (middle) and GBM20 (right) models. (**C**) Real time assessment of cellular confluency (normalized to t_0 values) in GBM1, GBM11, GBM20, and NP1 models before and after treatment (arrowheads) with DMSO (0.1%) or KHS101 (7.5 μM). A single experiment out of three biological replicates is shown (see file S2 for all data). ***, P<0.001, ****, P<0.0001, two-way ANOVA. (**D**) Dose-response curves (normalized to the DMSO control) and the corresponding IC50 values (μM, with 95% confidence intervals) are shown for the indicated cell models and KHS101 concentrations after a 5-day treatment period. Data are mean ± SD of three biological replicates.

Fig. 2. KHS101 selectively induces an autophagic and pro-apoptotic cell fate across a spectrum of GBM cell models. (**A**) EM and immunocytochemistry (Phase contrast (Phc); anti-LC3B; DAPI) images (scale bars: 5 and 25 μm, respectively) of GBM1 and NP1 cells 12 hours after KHS101 (7.5 μM) or DMSO (0.1%) treatments. (**B**) Immunocytochemistry (Phase contrast (Phc); anti-LC3B; DAPI) images (scale bar: 30 μm) of indicated cell models 12 hours after KHS101 (7.5 μM) or DMSO (0.1%) treatments. (**C**) Quantification of the LC3B-positive cytoplasmic area (%) 12 hours after treatment with KHS101 (at the indicated concentrations) or DMSO (D; 0.1%) using the specified cell models. (**D**) Quantification of CYTO-ID-positive

GBM1 cells 12 hours after treatment with DMSO (D; 0.1%) or KHS101 (at the indicated concentrations). (**E**) Kinetics of caspase 3/7 activation in GBM1 cells treated with KHS101 (7.5 μM) or DMSO (0.1%; data were normalized to t_o). (**F**) Relative caspase 3/7 activation (at the 48-hour time point) in response to DMSO (D; 0.1%) or KHS101 (K; 7.5 μM) in the specified cell models. N: negative control (K; 7.5 μM + pan-caspase inhibitor Z-VAD-FMK; 2 μM), P: Positive control (Staurosporine; 1 μM). Data are mean ± SD of three biological replicates, **, P<0.01, student's t-test (two tailed).

Fig. 3. KHS101 induces acute metabolic stress in GBM cells. (**A**) Kinetics of autophagy induction in CYTO-ID-labeled GBM1 cells upon KHS101 (7.5 μM) or DMSO (0.1%) addition. Data are mean ± SD of three biological replicates. (**B**) Hypergeometric gene enrichment test (left; OXPHOS and TCA cycle gene set enrichment is highlighted), and radar plot (right) indicating marked (>2-fold) alterations in cell cycle/mitosis, metabolic, and stemness pathways in GBM1 cells 24 hours after KHS101 treatment (7.5 μM) compared with the DMSO control (0.1%). FC indicates fold change. (**C**) qRT-PCR radar charts depicting KHS101-induced (7.5 μM) mRNA expression changes (in relation to the DMSO control; FC range: >-10 and <30) in GBM1 and GBM20 cell models (left, middle) and the lack of a similar response in NP1 cells, or by TACC3 silencing in GBM1 cells (right). (**D**) Metabolic phenogram. Basal extracellular flux rates (OCR and ECAR) of the specified cell types are shown in response to vehicle (DMSO; 0.1%) or KHS101 (7.5 μM) treatments. Quadrants indicate the specified metabolic phenotypes. Data are mean ± SD of three biological replicates.

Fig. 4. KHS101 impairs relative incorporation of glucose-derived carbon through glycolysis and the TCA cycle in GBM cells. (**A**) Gas Chromatography-Mass Spectrometry stable isotope analysis of methoximation and silylation-derivatized metabolites extracted from NP1 and GBM1 cells following a 4 hour treatment with KHS101 (7.5 μM) or DMSO (0.1%) in media containing U-^{13}C glucose. Graph shows the fractional enrichment (%) in the isotopologues of glucose. (**B to L**) Fractional enrichments of fructose 6-phosphate (F6P, B), dihydroxyacetone phosphate (DHAP, C), glyceraldehyde 3-phosphate (GAP, D), glycerol 3-phosphate (G3P, E), phosphoenolpyruvate (PEP, F), lactate (G), citrate (H), succinate (I), fumarate (J), malate (K), and aspartate (L). The X-axis indicates the mass isotopomers (which are designated as M0, M1, M2…Mn, where n is the number of labeled atoms in the molecule) in the specified metabolites (corrected for^{13}C natural abundance; lactate M2 not shown as enrichment above natural

abundance was not detected). Data are mean ± SEM of three biological replicates. *, P<0.05; **, P<0.01; ***, P<0.001; ****, P<0.0001, one-way ANOVA (Tukey post-hoc).

Fig. 5. KHS101 interacts with mitochondrial HSPD1. (**A**) Two-dimensional SDS/PAGE and Western blotting of GBM1 cell lysates (20-40% ammonium sulfate-precipitated fraction) detecting KHS101-BP-labeled protein in presence or absence of unlabeled KHS101 (as specified) after photocrosslinking (30 minutes) and biotin-tag labeling (click chemistry reaction using biotin-azide). Asterisk: 60 kDa. Right inlay shows the relative reduction of candidate compound-protein complex signal (%; spots 1-4) in presence of unlabeled KHS101. Median of three technical repeats (back dots) is shown. Spot 1 corresponded to HSPD1 (identified by proteomics analysis after protein spot excision). (**B**) Specific in vitro binding of recombinant human HSPD1 with biotinylated KHS101 (KHS101-bio) was detected by silver staining of SDS/PAGE gels in the presence/absence of unlabeled KHS101, precipitated with streptavidin-conjugated agarose beads. Asterisk: 60 kDa. (**C**) HSPD1 mitochondrial (M) to cytoplasmic (C) ratio in GBM1 and NP1 cells as assessed by immunoblot quantification.. Black dots represent biological replicates (Median ±SD is shown) **, P<0.01, student's t-test (2-tailed; equal variance). (**D**) Relative mitochondrial HSPD1 protein expression (%, normalized to control values as assessed by immunoblot) 6 hours after DMSO (0.1%, D) or KHS101 (7.5 μM, K) treatment in GBM1 cells. (**E**) HSPD1 mRNA expression (fold changes) in GBM1 cells treated with DMSO (D; 0.1%) or KHS101 (K; 7.5 μM). SD of three biological repeats (black dots) is shown.

Fig. 6. KHS101 induces HSPD1-dependent aggregation of metabolic enzymes. (**A**) HSPD1/HSPE1 substrate refolding activity in presence of KHS101 (IC50=14.4 μM). Data are mean ± SD of three replicates (**B**) HSPD1 complex substrate refolding activity in presence of HB072 (inactive KHS101 analog) and MC (mitochondrial HSPD1-binding compound). Data are mean ± SD of three replicates. (**C**) Left, silver staining of aggregated (pellet) and soluble (supernatant) mitochondrial fractions (solubilized with 0.5% NP-40) from NP1 and GBM1 cells treated with DMSO (D; 0.1%) or KHS101 (K; 7.5 μM) for 1 hour. Right, KHS101-induced protein enrichment as assessed for the aggregated/pellet (P) and soluble/supernatant (S) fractions in GBM1 versus NP1 cells. Data are GBM1/NP1 ratios of three biological replicates ± SD). **P<0.01, student's t-test (two-tailed, equal variance). Aggregated proteins were identified by mass spectrometry (table S2). . (**D**) KHS101-GBM protein aggregation represented in a predicted

(STRING) interaction network of proteins (homo sapiens; network edges: confidence; line thickness indicating strength of data support). Only GAPDH (italic) was shared between NP1 and GBM1 cells. Green, red, blue, and yellow colors represent enzymatic functions in protein folding, glycolysis, OXPHOS, and glycine metabolism, respectively. (**E**) Quantitative proteome analysis identifying differentially-regulated proteins and the specified enrichment sets in GBM1 cells treated with KHS101 (7.5 μM) for 1 hour. Data (logFC) are calculated from change in average protein levels between 1 hour and t_0. The -log10 of the Benjamini and Hochberg false-discovery-rate adjusted P-values were obtained from group-wise comparison (red line depicts P=0.05).

Fig. 7. KHS101 significantly attenuates GBM growth in vivo. (**A**) Confocal microscopic images (scale bar: 40 μm) and quantification of NAD(P)H autofluorescence (AF) in the vehicle (n=4) or KHS101 (n=4) treatment groups (using 3 different tissue sections per specimen). Nuclei were stained with propidium iodide (PI) (**B**) Immunocytochemistry-based quantification of HK2- and MKI67-positive tumor area in the vehicle (V; n=5) or KHS101 (K; n=6) treatment groups (using ≥3 different tumor sections per specimen). (**C**) Bean plot of MKI67 mRNA expression in single GBM1 cells 5 days after DMSO (D; 0.1%) or KHS101 (K; 7.5 μM) treatment. (**D**) Clonal growth capacity of individual GBM1 cells in presence of DMSO (D; 0.1%) or KHS101 (K; 1 or 7.5 μM). (**E**) Quantification of acellular/pyknotic areas in anterior GBM1 tumor sections; V: vehicle, K: KHS101. Dots represent individual tumor measurements. (**F**) GBM1 xenograft tumor size (% tumor area of sectioned brain) in vehicle- (V) or KHS101 (K)-treated animals assessed by Hematoxylin and Eosin staining in sequential brain areas (frontal to caudal; scale bar: 2 mm). Dots represent individual tumors. (**G**) Imaging and quantification of Vimentin-positive GBM1 xenograft tumor cells infiltrating the corpus callosum (CC) of the hemisphere contralateral to the injection site in animals of the vehicle (n=5) or KHS101 (n=6) treatment groups (using ≥3 sections per xenograft tumor). Dotted line indicates border of CC and Striatum (S). Scale bar: 300 μm. All boxplots show the 10-90 percentile and median, *, P<0.05; **, P<0.01, Mann Whitney U-test (one tailed).

Fig. 8. KHS101 treatment increases survival in the GBMX1 in vivo model. (**A**) Survival analysis of the specified glioma subtype categories and median preset thresholds for HSPD1 mRNA expression (using default settings available from http://www.betastasis.com/glioma/rembrandt/kaplan_meier_survival_curve/). (**B**) Kaplan-Meier

(log-rank test) analysis of GBMX1 tumor-carrying animals. Tumors were established over a 2 week period followed by 10 weeks of vehicle (n=8) or KHS101 (n=8) treatment. (**C**): Kaplan-Meier (log-rank test) analysis of GBMX1 tumors that were allowed to establish over a 6 week period followed by continuous vehicle (n=4) or KHS101 (n=5) treatment until the endpoint (arrowhead). (**D**) GBMX1 xenograft tumor size (% tumor area of sectioned brain) in vehicle- or KHS101-treated brains at their respective endpoints (shown in C) assessed by Hematoxylin and Eosin staining (using ≥4 sections per specimen; scale bar: 2 mm). Boxplot shows the 10-90 percentile and median, and dots represent individual (brain section) values. **, $P<0.01$, Mann Whitney U-test (one tailed).

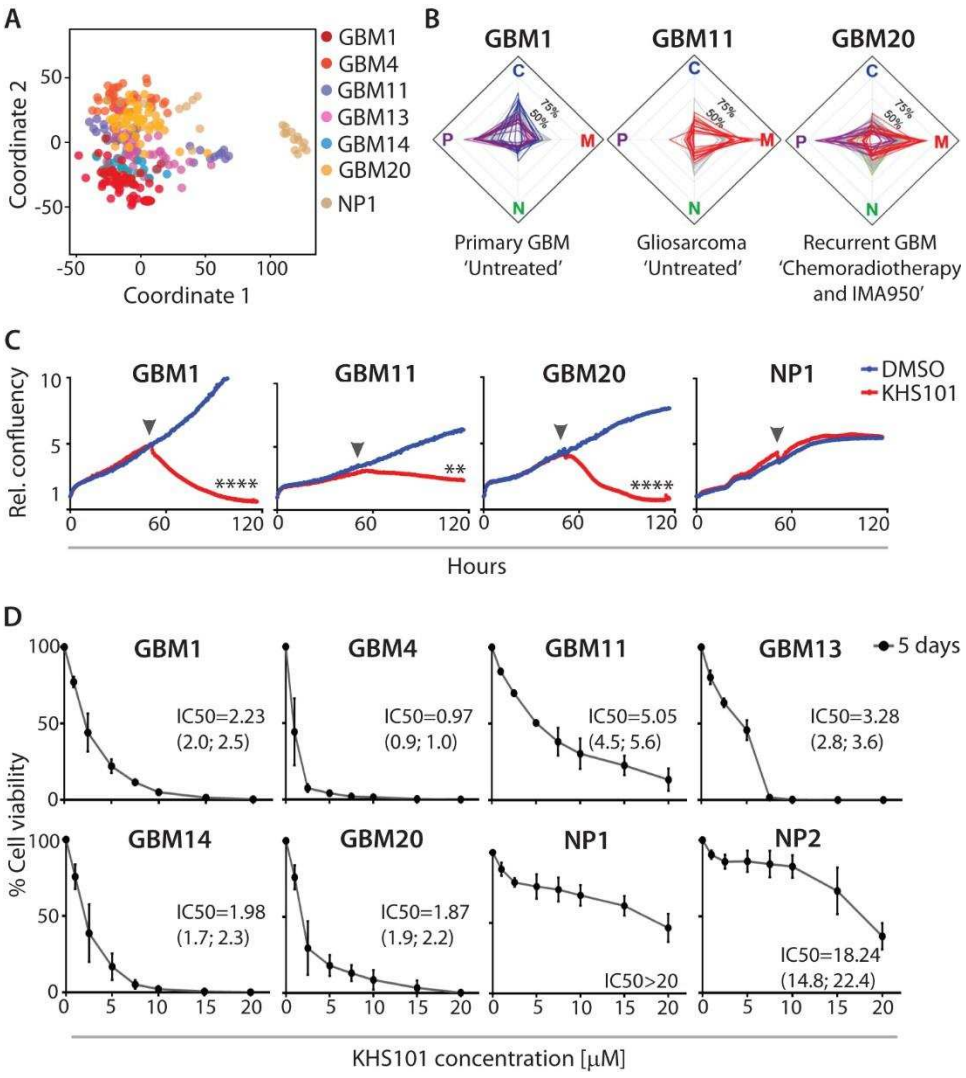

Fig. 1. KHS101 exhibits cytotoxicity in molecularly-diverse GBM models.

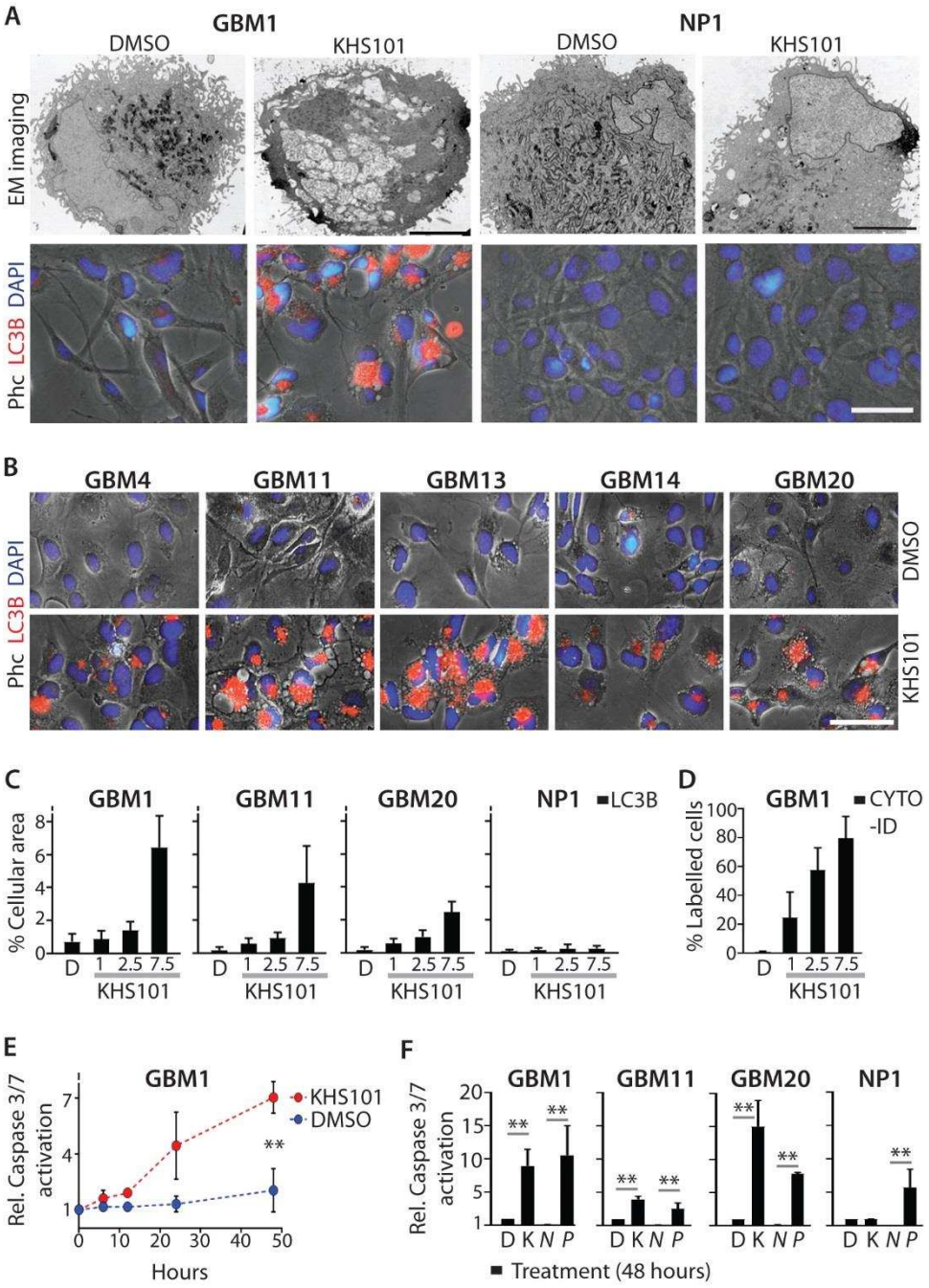

Fig. 2. KHS101 selectively induces an autophagic and pro-apoptotic cell fate across a spectrum of GBM cell models.

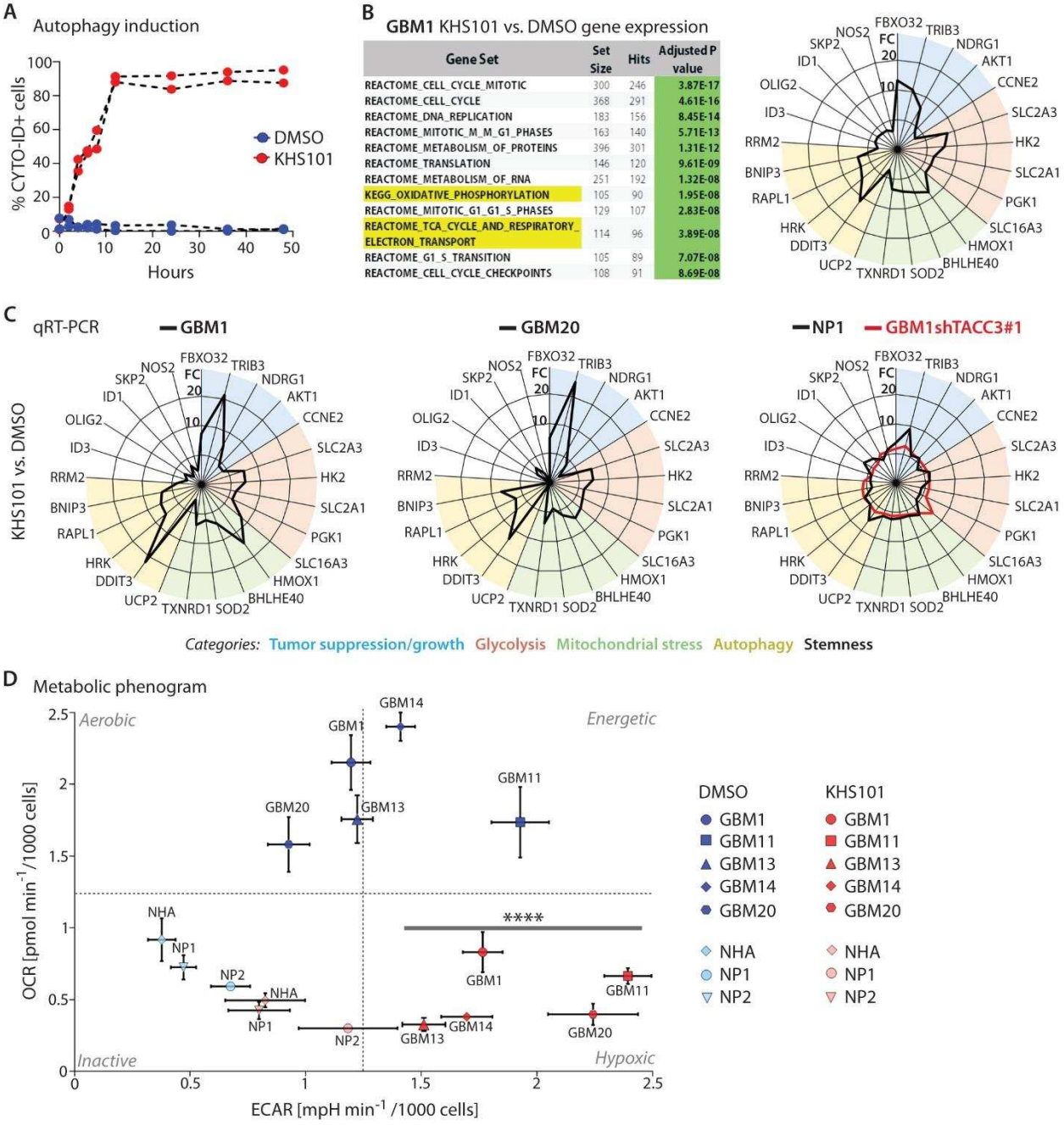

Fig. 3. KHS101 induces acute metabolic stress in GBM cells.

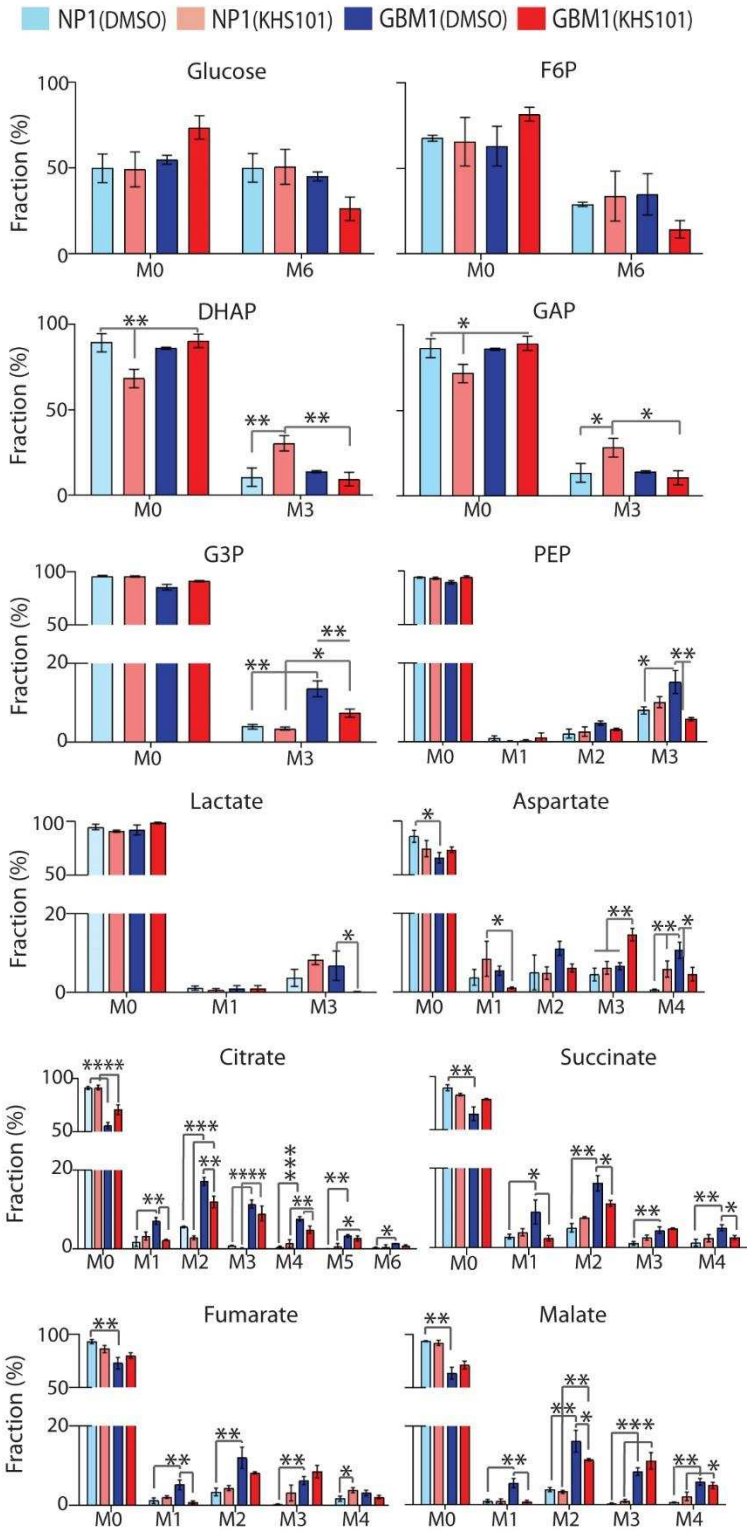

Fig. 4. KHS101 impairs relative incorporation of glucose-derived carbon through glycolysis and the TCA cycle in GBM cells.

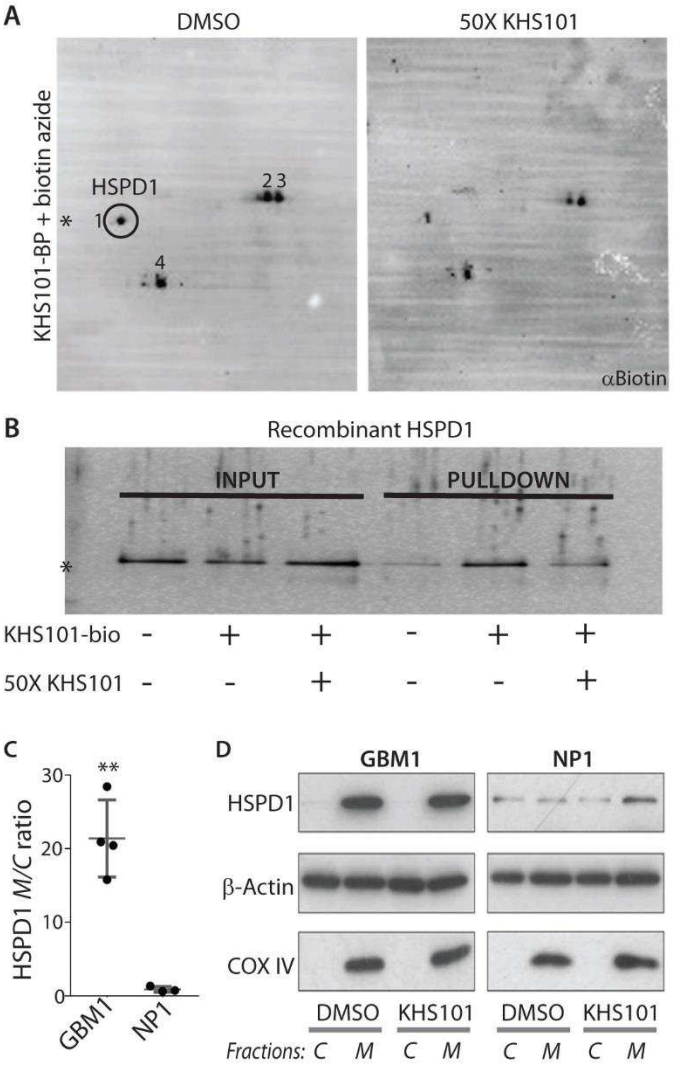

Fig. 5. KHS101 interacts with mitochondrial HSPD1.

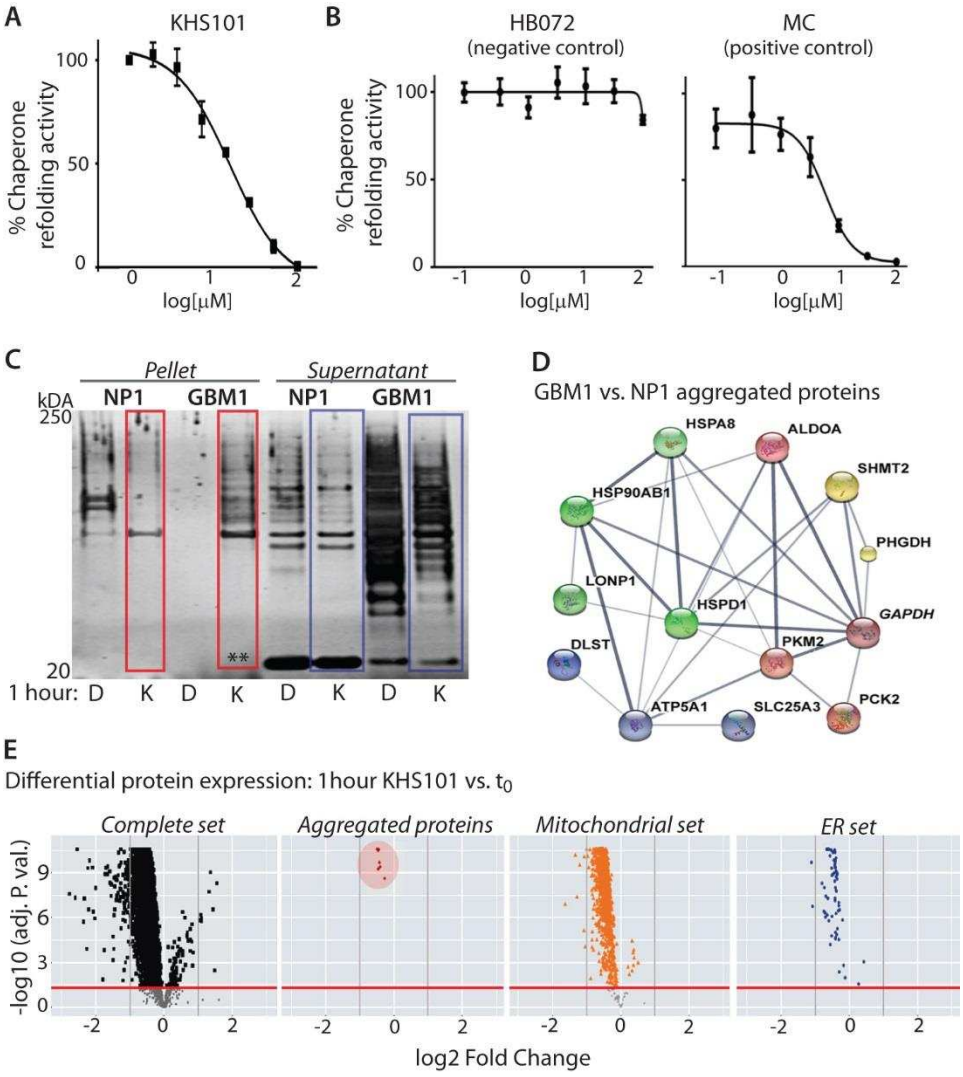

Fig. 6. KHS101 induces HSPD1-dependent aggregation of metabolic enzymes.

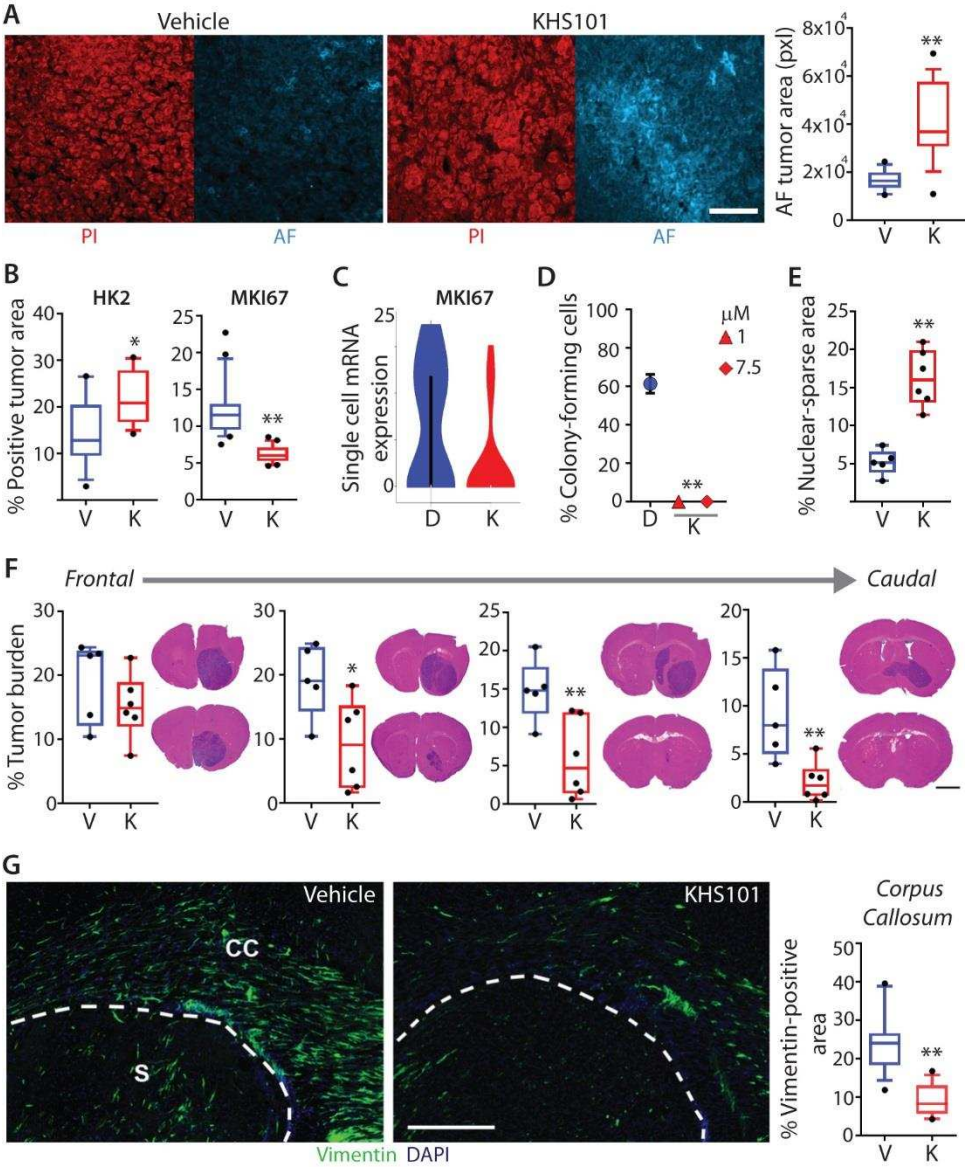

Fig. 7. KHS101 significantly attenuates GBM growth in vivo.

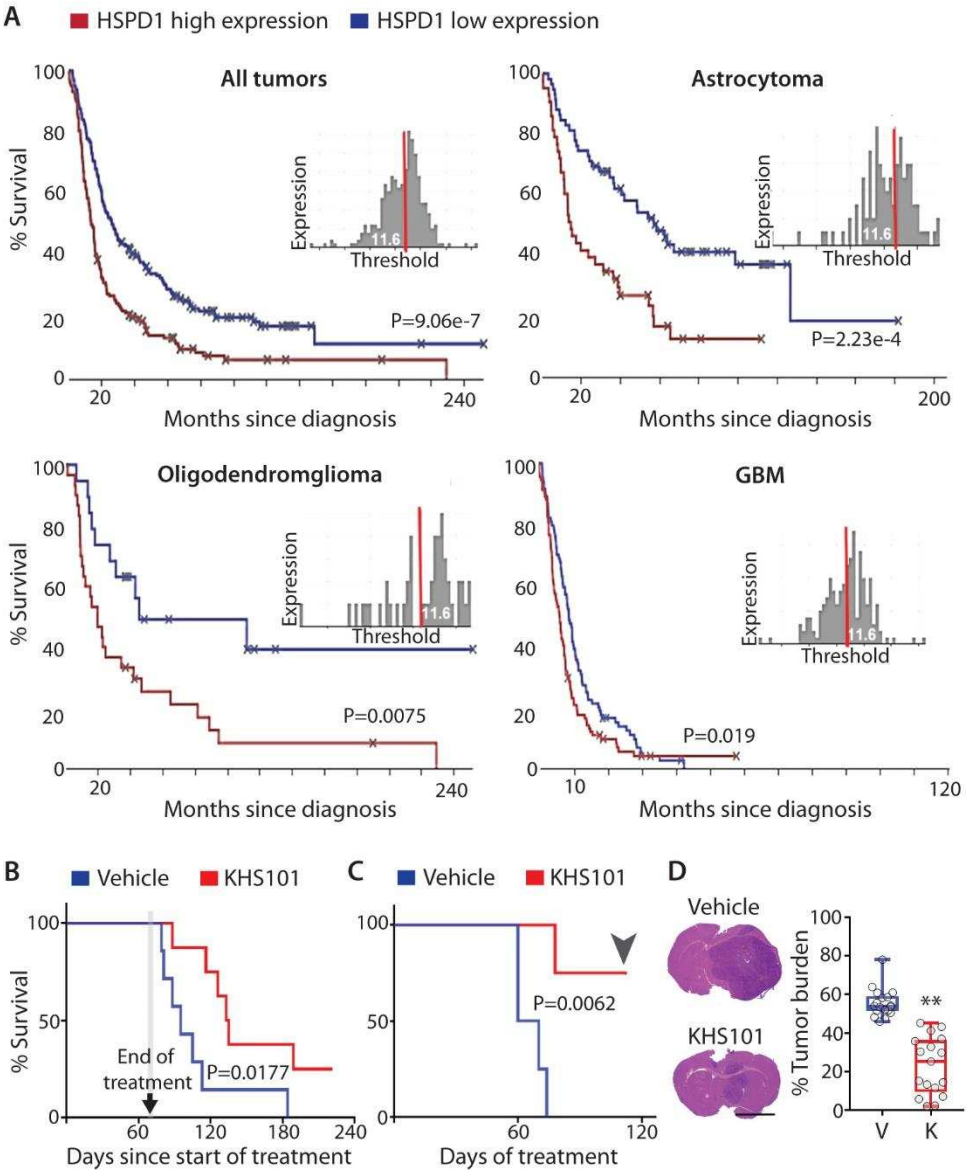

Fig. 8. KHS101 treatment increases survival in the GBMX1 in vivo model.